

# Analysis of different propeller ventilation mechanisms by means of RANS simulations

Andrea Califano      Sverre Steen

Rolls-Royce University Technology Center 'Performance in a Seaway'  
Department of Marine Technology, Norwegian University of Science and Technology

## ABSTRACT

Based on the experiments of Shiba (1953) and Koushan (2006) an analysis of different types of propeller ventilation was performed by means of numerical simulations.

The aim of this work is to analyse the ventilation mechanisms, whose deeper understanding would improve the ability to predict them. Ventilation can seriously damage mechanical components of an engine, eventually leading to its failure.

The commercial RANS code Fluent (2006) has been used to solve the viscous, incompressible, two-phase flow. The rotation of the propeller has been implemented both with a Multiple Reference Frame model and using Sliding Mesh. Results of a fully ventilating case, in terms of blade and propeller loadings, are presented and discussed with the aid of flow visualization at different angular positions.

For a well submerged propeller, a discussion about ventilation induced by a free-surface vortex is presented.

## Keywords

Blade, RANS, propeller, thruster, ventilation.

## 1 INTRODUCTION

This work was performed in the framework of a numerical study aiming at modeling the ventilation phenomenon, which has been recognized to be important for marine screws, rudders and submerged hydrofoils (see experiments by Shiba, 1953; Nishiyama, 1961; Koushan, 2006). During the operation of a vessel, ventilation can seriously damage mechanical components of an engine, leading to its failure, due to instability and sudden change in thrust and torque, and consequently in the sudden increase in revolutions. Fluctuating propeller loadings occur more often during operations of dynamic positioning, characterized by low advance speed and high propeller loadings.

The effect of ventilation on average thrust and torque of propellers operating in waves is discussed by Faltinsen et al. (1981), Minsaas et al. (1983) and Minsaas et al. (1987). In order to get a better insight into propeller ventilation, experiments were carried out on a wide range of configurations (Koushan, 2006).

Previous numerical works dealing simultaneously with

propeller and free-surface flow are mainly devoted to partially submerged propellers. These propellers are surface-piercing already at rest, and their application is only for high-speed vessels. Young and Kinnas (2004) with a Boundary Element Method and Caponnetto (2003) with RANS have successfully reproduced the dynamic loads measured during the experiments performed by Olofsson (1996) on partially-submerged propellers. The authors are not aware of other numerical works reproducing the interaction of a fully submerged propeller with the free surface (not surface-piercing).

A numerical modeling of the experiments performed by Koushan (2006) has been started studying a case showing full ventilation. This run was performed at a submergence ratio  $h/R = 1.4$  and at an advance ratio  $J = 0.1$ , defined as:

$$J = \frac{U}{nD}$$

The numerical domain of this configuration is shown in Figure 1 and corresponds to a shaft submergence of 1.4 times the propeller radius  $R$ , resulting in a minimum clearance of the propeller disc from the undisturbed free-surface of 0.05 m.

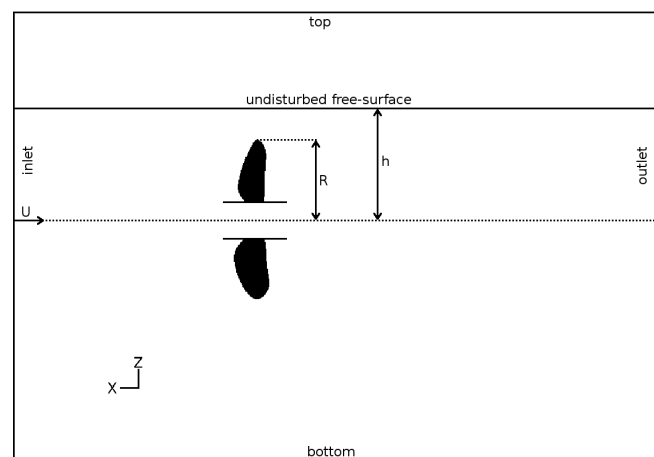


Figure 1: Numerical domain

The propeller chosen for the computations has been extensively used for various kinds of ventilation tests, with

and without the presence of the duct. The model has thus a generic design, representing a typical propeller which can be used in different regimes. While the experiments are performed with a pulling thruster, only the propeller is modelled in the numerical simulations. The propeller is right-handed, with a diameter  $D$  of 0.25 m and a hub diameter  $D_{hub}$  of 0.06 m. Design pitch ratio  $P/D$  is 1.1 and blade area ratio  $EAR$  0.595.

In order to verify the numerical error of the implemented simulation, a sensitivity analysis was performed in open water conditions, and its results validated against the available experiments, for a wide range of advance ratios.

## 2 VENTILATION MECHANISM

Shiba (1953) has studied the ventilation mechanism in details, performing preliminary experiments on surface-piercing cylinders and hydrofoils, and extensively analysing the parameters affecting propeller ventilation, for which he gives a phenomenological description (Shiba, 1953, chap IV, § 2, page 38):

*”Air-drawing of a marine propeller signifies the penetration of atmosphere through an air hole or along the blade surface in contact with atmosphere into the dead water region or sub-atmospheric region on the upper surface of propeller blades.”*

This definition contains already the main features of the propeller ventilation mechanism, which occurs in presence of the atmosphere, and can reach the propeller through an *”air hole”* or *”along the blade surface in contact with atmosphere”*.

The presence of the propeller modifies the undisturbed inflow superimposing an induced velocity field, which is radially pulling the surrounding flow towards the propeller (see Greenberg, 1972, for the streamtubes of a heavily loaded actuator disk). In the vicinity of the free surface, these induced velocities are able to deform the interface between the two phases, pulling it towards the propeller, as seen in the experiments performed by Paik et al. (2008).

The two different mechanisms feeding air to the propeller can be better understood through the visualization presented by Koushan (2006).

For moderate submergence ratios (Koushan, 2006, Figure 15,  $h/R = 1.4$ ) the deformation of the free surface is such that the blades become surface-piercing. From this time on, air is continuously drawn from the free surface down to the propeller disc.

A different mechanism occur for a well submerged propeller (Koushan, 2006, Figure 11,  $h/R = 2.6$ ), because the propeller is farther away from the free surface. This implies that the induced velocities exerted by the propeller on the free surface are smaller (reduced pulling effect as a result of increased distance), besides an increased distance already in undisturbed conditions. The formation of a vortex can be seen on the free surface, and in this case

ventilation is started after this funnel reaches the propeller tip, turning into an air hole connecting the free surface with the propeller.

## 3 NUMERICAL METHOD

The commercial RANS code Fluent (2006) has been used to solve the viscous, incompressible, two-phase (air and water) flow. The undisturbed free-surface elevation is assigned both at the inlet and outlet boundaries. At the inlet the free stream velocity is also specified.

The momentum equation is solved with a second order up-wind scheme. The Body Force Weighted discretization algorithm is used to interpolate the node values of the pressure from the cell values, as required by the solver. The pressure-velocity coupling is achieved using a SIMPLE algorithm. A first order implicit scheme is used to follow the time evolution. The free surface evolution is handled using an implicit formulation of the Volume Of Fluid method with a modified High Resolution Interface Capturing scheme. Further details about the solver can be found in the Fluent manual (Fluent, 2006).

The undisturbed free surface elevation is assigned both at the inlet and outlet boundaries. At the inlet the free stream velocity is also specified. A zero flux of all quantities is enforced across the top and bottom boundaries. A no-slip condition on the wall is set.

The grid is fully unstructured in the rotating domain, with a superimposed prismatic layer close to the walls, in order to better capture the boundary layer (Rhee and Joshi, 2006). Prisms are generated upstream and downstream the rotating domain, whereas the remaining cells are fully structured. A total of about 2.35 million cells was used, most of them located around the propeller and across the interface between the two phases. A typical size for the cell at the free surface is 5 mm. An ensemble view of the grid used on the domain’s boundaries is shown in Figure 2.

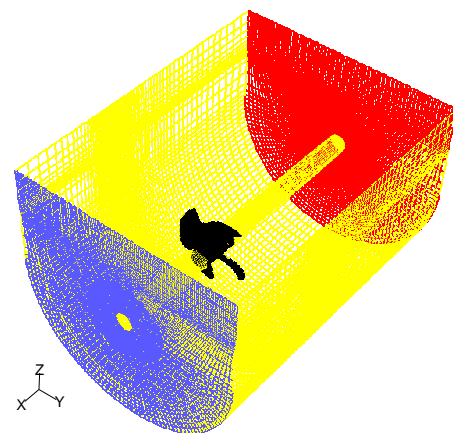


Figure 2: Mesh topology on the domain boundaries

A close up of the mesh topology on the blade is given in

Figure 3.

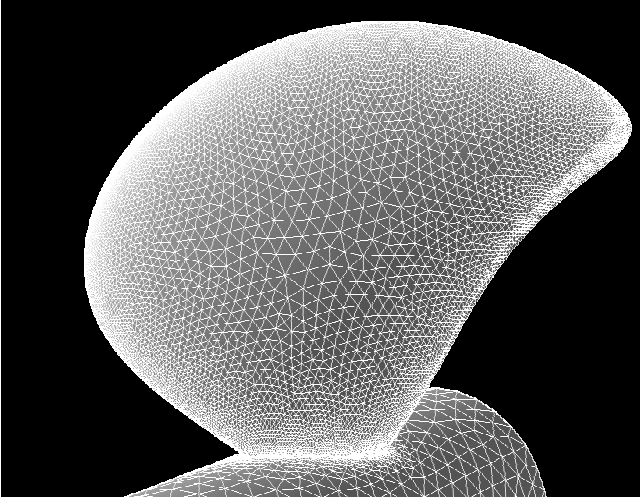


Figure 3: Mesh topology on the blade wall

While a SST  $k - \omega$  model (Menter, 1994) was used in open water conditions (§ 4.1), turbulence was removed when simulating the free-surface flow (§ 4.2). Performing a laminar computation helped reducing the computational time, and such an approximation is deemed as of minor importance for the present study. This assumption and the background for the chosen numerical model are discussed by Califano (2008), who investigated the importance of the parameters affecting the simulation of a lifting surface close to the free surface.

### 3.1 Propeller rotation

The propeller geometry is embedded in a cylindrical domain, as shown in Figure 4.

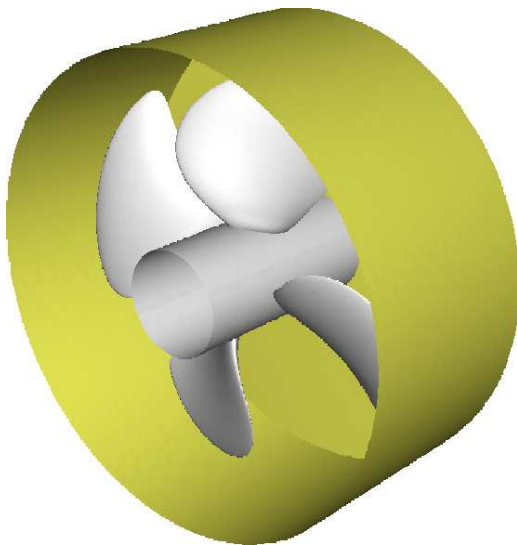


Figure 4: Rotating domain

The rotation of this domain was achieved both with a Multiple Reference Frame (MRF) model and using Sliding Mesh (SM).

In the MRF model the propeller is fixed, while its rotation is taken into account using a local reference frame rotating at the desired propeller rate. The corresponding equations of motion are modified to incorporate the additional acceleration terms arising from the use of a rotating reference frame. This approach is most suitable when the interaction between stationary and moving parts are quasi-steady.

When the unsteadiness of the aforementioned interaction becomes important, a Sliding Mesh model has to be adopted, accounting for the relative motion of stationary and rotating components. The increased accuracy is achieved at the expense of a higher computational time.

## 4 RESULTS

The results obtained for the open water test and including the free surface are discussed in the following sections.

### 4.1 Open water

A validation and verification activity in open water was performed before including the free surface.

Propeller characteristics can be presented in dimensionless form, in terms of thrust  $K_T$ , torque  $K_Q$  and efficiency  $\eta$ , defined in the following equations:

$$K_T = \frac{T}{\rho n^2 D^4}, \quad K_Q = \frac{T}{\rho n^2 D^5}, \quad \eta = \frac{J K_T}{2\pi K_Q}$$

Figure 5 shows the propeller characteristics as a function of the velocity of advance  $J$ , for the present simulations, compared with the available experiments and BEM computations.

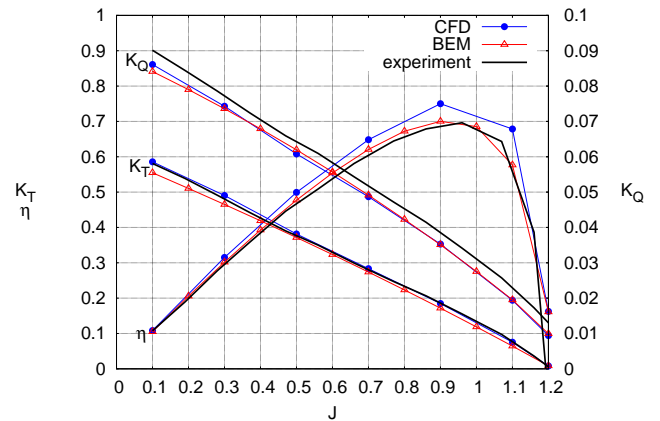


Figure 5: Dimensionless thrust, torque and efficiency in open water: comparison between experiments (—), CFD (—●—) and BEM (—△—)

The corresponding numerical values are reported in Table 1 for the thrust coefficient and in Table 2 for the torque coefficient, both including the relative error with respect to the experiments.

$J$	exp	CFD	$\Delta\%$	BEM	$\Delta\%$
0.1	0.5915	0.5857	0.98%	0.5547	6.22%
0.3	0.4938	0.4904	0.69%	0.4651	5.81%
0.5	0.3941	0.3815	3.20%	0.3716	5.71%
0.7	0.2929	0.2834	3.25%	0.2738	6.53%
0.9	0.1929	0.1848	4.19%	0.1716	11.04%
1.1	0.0811	0.0752	7.29%	0.0643	20.78%
1.2	0.0143	0.0080	44.24%	0.0084	41.66%

Table 1: Thrust coefficient: comparison of CFD and BEM results with experiments, including the relative error.

$J$	exp	CFD	$\Delta\%$	BEM	$\Delta\%$
0.1	0.0885	0.0861	2.69%	0.0841	4.93%
0.3	0.0768	0.0743	3.24%	0.0736	4.16%
0.5	0.0649	0.0608	6.28%	0.0620	4.51%
0.7	0.0521	0.0487	6.55%	0.0491	5.70%
0.9	0.0387	0.0353	8.89%	0.0351	9.38%
1.1	0.0230	0.0194	15.80%	0.0195	15.32%
1.2	0.0136	0.0094	31.08%	0.0099	27.19%

Table 2: Torque coefficient: comparison of CFD and BEM results with experiments, including the relative error.

The thrust coefficient computed from CFD is in satisfactory agreement with the available experiments, for the whole range of advance ratios. For high propeller loadings, i.e. for low advance ratios, the difference in thrust with respect to the experiment is very small, about 1% for  $J=0.1$ , the case which has been further investigated including the free surface in Section 4.2.

The torque coefficient shows a systematic under-estimation of the experimental data, which is also seen in the BEM. An error in the torque coefficient has been widely documented in other RANS simulations (Bulten and Oprea, 2005; Rhee and Joshi, 2006; Berchiche and Janson, 2008), where an over-prediction was encountered instead.

The prediction of thrust and torque is related to lift and drag predictions of a 2D profile. Using standard two-equations turbulence models, such as  $k-\epsilon$  and  $k-\omega$ , lift is predicted well, whereas the drag shows a sensible deviation. Bulten and Oprea (2005) attribute this trend to an error in the evaluation of the stagnation point pressure, while for Rhee and Joshi (2006) this can be associated to the lack of a proper laminar-to-turbulent transition model. The correct location of the turbulent transition point along the chord-line can not be predicted by fully turbulent models, and this uncertainty leads to an error when evaluating the drag for a 2D profile and the torque for a propeller.

#### 4.2 Ventilation

The simulation in presence of the free surface was started using the Multiple Reference Frame model. After the sim-

ulation had reached a stable solution, both for the forces and the phase volume fraction, the Sliding Mesh model was applied. Figure 6 shows the results of the SM, in terms of propeller thrust and torque coefficient. Vertical grid lines are located at the same azimuthal position for the blade passage, thus representing the number of propeller revolutions.

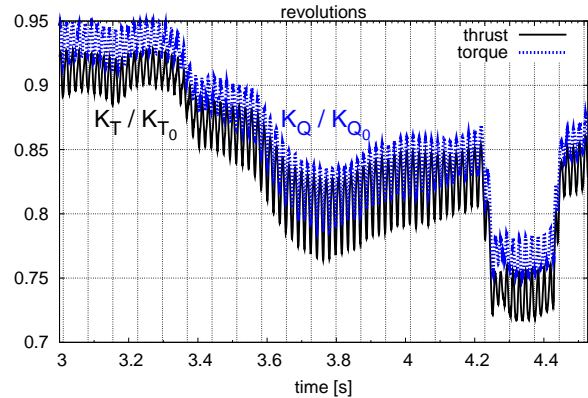


Figure 6: Propeller thrust (—) and torque (- -) coefficient, scaled with the corresponding open water coefficients, as a function of time.

Both thrust and torque follow the same trend, having regular oscillations with a frequency which is four times the shaft frequency. The amplitude of these high-frequency oscillations is about 5% of the corresponding open water average value. The average values have less pronounced oscillations. After an initially constant behaviour, thrust and torque decrease due to an increasing suction of air. The sudden thrust loss visible between 4.2 and 4.4 sec follows the reduction of the relaxation factors. The variation in the time series can be related to the large fluctuations observed during the experiments, as shown in Figure 7, where the thrust ratio of the whole propulsor during a time interval equal to the one used in Figures 6 and 8 is plotted.

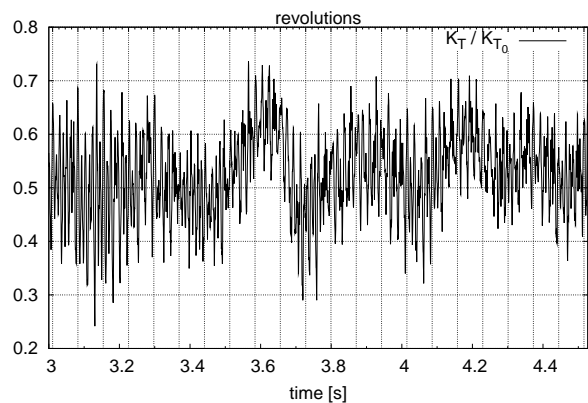


Figure 7: Experimental values of the propulsor thrust ratio, as a function of time.

Figure 8 shows the propeller and blade thrust coefficients, scaled with the open water propeller thrust coefficient  $K_{T_0}$ .

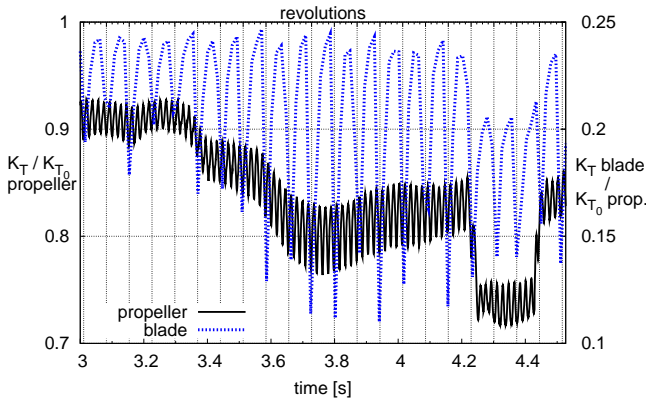


Figure 8: Propeller (—) and blade (- -) thrust coefficient, scaled with the open water propeller thrust coefficient, as a function of time.

During one revolution, the blade thrust experiences one oscillation cycle, whereas the propeller shows four cycles in the same oscillation period. While the propeller thrust is oscillating with an amplitude of 5% of its nominal value, the single blade is experiencing larger oscillations, up to 15% of the propeller nominal thrust, corresponding to more than 50% of the blade nominal value.

This behavior is clearly visible in Figure 9, which shows the blade thrust coefficient ratio during one propeller revolution, as a function of the azimuthal position of the blade axis, both for the Multiple Reference Frame and Sliding Mesh models.

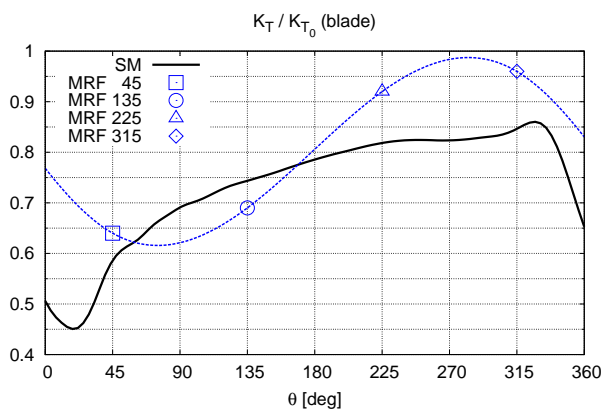


Figure 9: Blade thrust coefficient ratio during one revolution, for the Multiple Reference Frame (—) and Sliding Mesh (- -) models

Both models show a reduced thrust in the first half revolution against an increased value in the second one, where the thrust is still below its nominal value. The SM model is able to capture the sudden thrust loss from its peak value,

in proximity of the free surface, starting around 330 deg. This fall continues almost linearly until reaching its lowest value after crossing the free surface, around 20 deg, where the thrust is reduced to one-half. Subsequently, the thrust increases continuously, rapidly for the first 20 deg, and with a lower slope in the remaining part of the rotation, until reaching again its peak value. Instantaneous flow field for different azimuthal position can be seen in Figure 12 at the end of the paper.

The results from the MRF model are discrete points located on the four fixed blade axis positions. An interpolated spline curve represented with a dashed line goes through these points, showing the trend of the thrust during one propeller revolution. Despite being built on only four points, this trend follows qualitatively well the results obtained using the SM model, the latter being more computationally demanding.

Figure 10 shows a comparison of the experimental results (Koushan, 2006), obtained averaging each azimuthal position, with the computed blade thrust using sliding mesh.

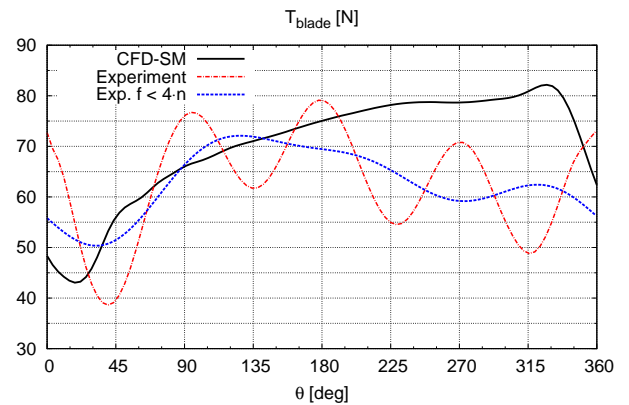


Figure 10: Blade thrust during one revolution. Comparison of the present results (—) with raw (- -) and filtered (- · -) experimental data

Experimental data show clear oscillations in the blade-frequency range. Oscillations with frequencies which are multiple-valued of the propeller frequency ( $n, 2 \cdot n, 3 \cdot n, \dots$ ) can be seen both in experimental tests and numerical simulations, but the authors are not aware of previous works showing oscillations in the blade-frequency range with amplitude as high as the present one. One could presume that a systematic error is affecting the mechanical response of the system, nevertheless other flow features might influence the ventilating flow object of this investigation. Since a clear statement about whether these blade-frequency oscillations are related to mechanical properties or fluid-dynamic phenomena, experiments are presented both in their original format and filtered with a low-pass filter allowing frequencies up to three times the propeller frequency.

The blade thrust computed from the present simulation

follow quite well the filtered experimental results during the first half revolution. Both curves detect a lower peak value around 30 deg and follow the subsequent increase in thrust. This agreement disappears around 150 deg, where the thrust obtained from the CFD continues to rise, whereas the experimental thrust begins to decrease.

Despite this general disagreement during the second half revolution, a slight down-facing hump is visible in both results around 270 deg. The peak value detected from the numerical simulation around 330 deg reflects the corresponding up-facing hump shown by the experiments. Subsequently, both curves predict a thrust decrease converging towards a common low-peak value.

An explanation of the found disagreement could be attained comparing the instantaneous flow field of both cases. Figure 11 at the end of the paper shows typical flow fields around the propeller at a certain time instant, for the CFD simulation (Figure 11a) and the corresponding experiment (Figure 11b). Propeller blades in Figure 11a are colored with the water volume fraction, while the free surface is colored with its height, taken in the direction of gravity.

The CFD simulations are able to reproduce the deformation of the free surface and the resulting air-drawing. While the first half revolution shows an air content similar to the one seen in the experiments, air is soon dispersed, such as its content in the second half revolution is almost zero. The corresponding propeller thrust will thus increase towards its nominal values. Experiments show a larger presence of air all around the propeller disc, both in azimuthal and radial directions. In proximity of the free surface CFD is predicting a correct air content, which is more and more reduced during the rotation. This discrepancy could be explained in two manners, related to the discretization and the flow features adopted for the numerical simulations. A coarse discretization of the domain could play an important role affecting the lack of transport of air among adjacent cells. Experimental data are available after ventilation has occurred. The time to reach the ventilating state depends on the tested configuration, but the time lasted before starting the recordings is higher than the numerical simulation time (less than 5 seconds). Although the flow field seen in the simulations appears periodically stable, ventilation might still be not fully developed, such as a longer simulation time could lead to a larger spreading of air around the propeller disc.

The present CFD analysis was not able to predict ventilation for a well submerged case, phenomenon which has been described in § 2.

In this case ventilation is started from an air hole which is open as a result of the vortex on the free surface, whose formation was not detected by the present CFD analysis. The formation of the free-surface vortex is not fully understood and the difficulty to detect it numerically can be ascribed to the lack of important physical features, such as turbulence

and surface tension, besides adopting a mesh which might be too coarse at the interface. The simulation time (less than 5 seconds) is also deemed as too short to establish a stable vortex. Surface tension is generally accounted for with the dimensionless Weber number:

$$We = n D \sqrt{\frac{\rho}{S} D}$$

In the present case  $We > 200$ , which is higher than 180, described by Shiba (1953) as the limit above which the influence of surface tension can be neglected. Nevertheless, surface tension might play an important role for well submerged propellers, leading to instabilities which might eventually cause the formation of a free-surface vortex.

## 5 CONCLUDING REMARKS

A validation and verification analysis of the propeller in open water has been carried out showing for all range of advance ratios a good agreement for the thrust coefficient, and a quasi-systematic error in the torque coefficient.

The air drawing of a submerged marine propeller close to the free surface has been simulated and the obtained results compared with experiments by Koushan (2006).

The present analysis shows a satisfactory agreement with the filtered experimental data during the first half revolution, both in terms of thrust forces and air content. Two factors have been identified as responsible for the reduced air content in the second half propeller revolution, with respect to the corresponding experimental test: short simulation time and a coarse mesh. Their influence could not be tested because of the available computer resources, but they shall be further investigated. The choice of the under-relaxation factors has shown to affect the numerical solution. Its influence with a more thorough analysis to the numerical parameters is also planned.

Another type of propeller ventilation, induced from the funnel formation on the free surface, could not be achieved by simulation. This phenomenon is observed during experiments for well submerged propellers and require longer time for the formation of the funnel. The present numerical scheme is not able to capture it and efforts should be made to understand its physical features in order to implement a suitable numerical model.

No trace of the blade-frequency component has been found in the present simulations. Additional tests will be performed using a different instrumentation in order to assess the influence of the mechanical system.

## Acknowledgment

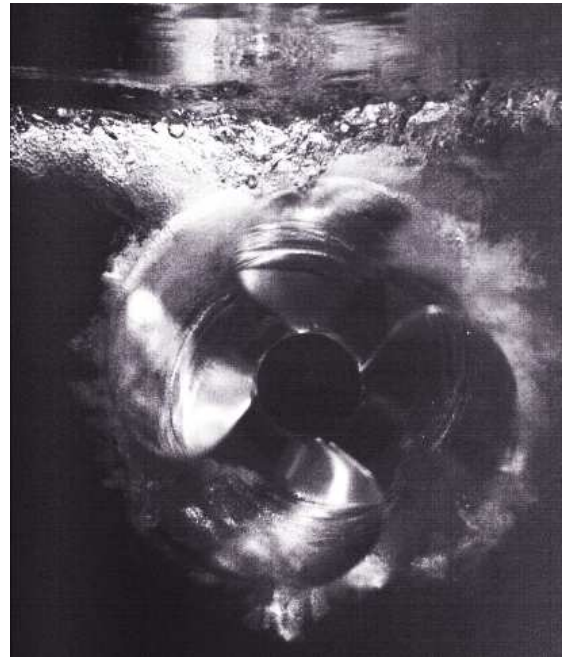
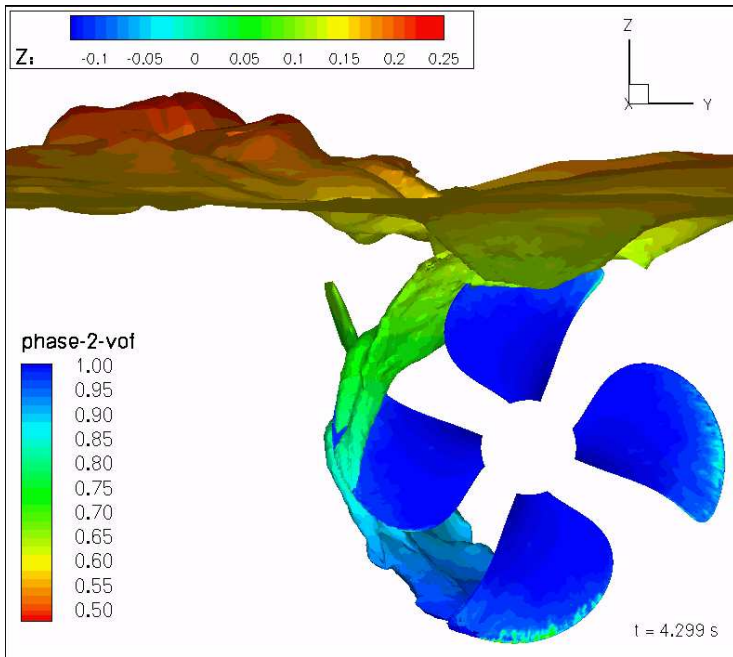
The authors gratefully acknowledge the Rolls-Royce University Technology Center in Trondheim for supporting the present research. This project was partially supported by the Norwegian HPC project NOTUR that granted access to its computer facilities. The authors also acknowledge Dr. K. Koushan for providing experimental data and Dr. V. Krasilnikov for providing the results of the BEM.

## Nomenclature

$\eta$	Propeller efficiency
$\rho$	Water density
$D$	Propeller diameter
$D_{hub}$	Hub diameter
$EAR$	Blade area ratio
$h$	Propeller axis submergence
$h/R$	Submergence ratio
$J$	Advance ratio
$K_{Q_0}$	Torque coefficient in open water
$K_Q$	Torque coefficient
$K_{T_0}$	Thrust coefficient in open water
$K_T$	Thrust coefficient
$n$	Rotation rate
$P/D$	Pitch ratio
$Q$	Propeller torque
$R$	Propeller radius
$T$	Propeller thrust
$U$	Free-stream velocity
$We$	Weber number

## REFERENCES

- Berchiche, N. and Janson, C.-E. (2008). Grid influence on the propeller open-water performance and flow field. Ship Technology Research, 55(1):87 – 96.
- Bulten, N. and Oprea, I. (2005). Explanation of deviations in torque prediction for waterjets and propellers with rans codes. In Marine CFD 2005.
- Califano, A. (2008). Influence of the near wall treatment on the flow features around a two-dimensional hydrofoil close to the free surface. In 11th Numerical Towing Tank Symposium - NuTTS'08.
- Caponnetto, M. (2003). Rans simulations of surface piercing propellers. In 6th Numerical Towing Tank Symposium - NuTTS'03.
- Faltinsen, O. M., Minsaas, K. J., Liapis, N., and Skjørdal, S. O. (1981). Prediction of resistance and propulsion of a ship in a seaway. In Proceedings of 13th symposium on naval hydrodynamics, pages 505 – 529.
- Fluent (2006). Fluent 6.3 User's Guide. Fluent Inc.
- Greenberg, M. (1972). Nonlinear actuator disk theory. Zeitschrift für Flugwissenschaften, 20(3):90 – 8.
- Koushan, K. (2006). Dynamics of ventilated propeller blade loading on thrusters. In World Maritime Technology Conference - WMTC'06.
- Menter, F. (1994). Two-equation eddy-viscosity turbulence models for engineering applications. AIAA Journal, 32(8):1598 – 1605.
- Minsaas, K. J., Faltinsen, O. M., and Persson, B. (1983). On the importance of added resistance, propeller immersion and propeller ventilation for large ships in a seaway. In Proceedings of International Symposium on Practical Design of Ships and other Floating Structures - PRADS'83.
- Minsaas, K. J., Thon, H. J., Kauczynski, W., and Karlsen, S. I. (1987). Estimation of required capacity for operation of offshore vessels under severe weather conditions. In Proceedings of International Symposium on Practical Design of Ships and other Floating Structures - PRADS'87.
- Nishiyama, H. (1961). Air-drawing and ventilating flow characteristics of shallowly submerged hydrofoil sections. American Society of Naval Engineers – Journal, 73(3):593 – 602.
- Olofsson, N. (1996). Forces and Flow Characteristics of a Partially Submerged Propeller. PhD thesis, Chalmers Tekniska Högskola.
- Paik, B.-G., Lee, J.-Y., and Lee, S.-J. (2008). Effect of propeller immersion depth on the flow around a marine propeller. Journal of Ship Research, 52(2):102 – 113.
- Rhee, S. H. and Joshi, S. (2006). Computational validation for flow around a marine propeller using unstructured mesh based navier-stokes solver. JSME International Journal, Series B: Fluids and Thermal Engineering, 48(3):562 – 570.
- Shiba, H. (1953). Air-drawing of marine propellers. Technical Report 9, Transportation Technical Research Institute.
- Young, Y. L. and Kinnas, S. A. (2004). Performance prediction of surface-piercing propellers. Journal of Ship Research, 48(4):288 – 304.



(a) CFD: propeller blades are colored with water volume fraction, while the free surface with its height, taken in the direction of gravity.

(b) Experiments.

Figure 11: Instantaneous flow field

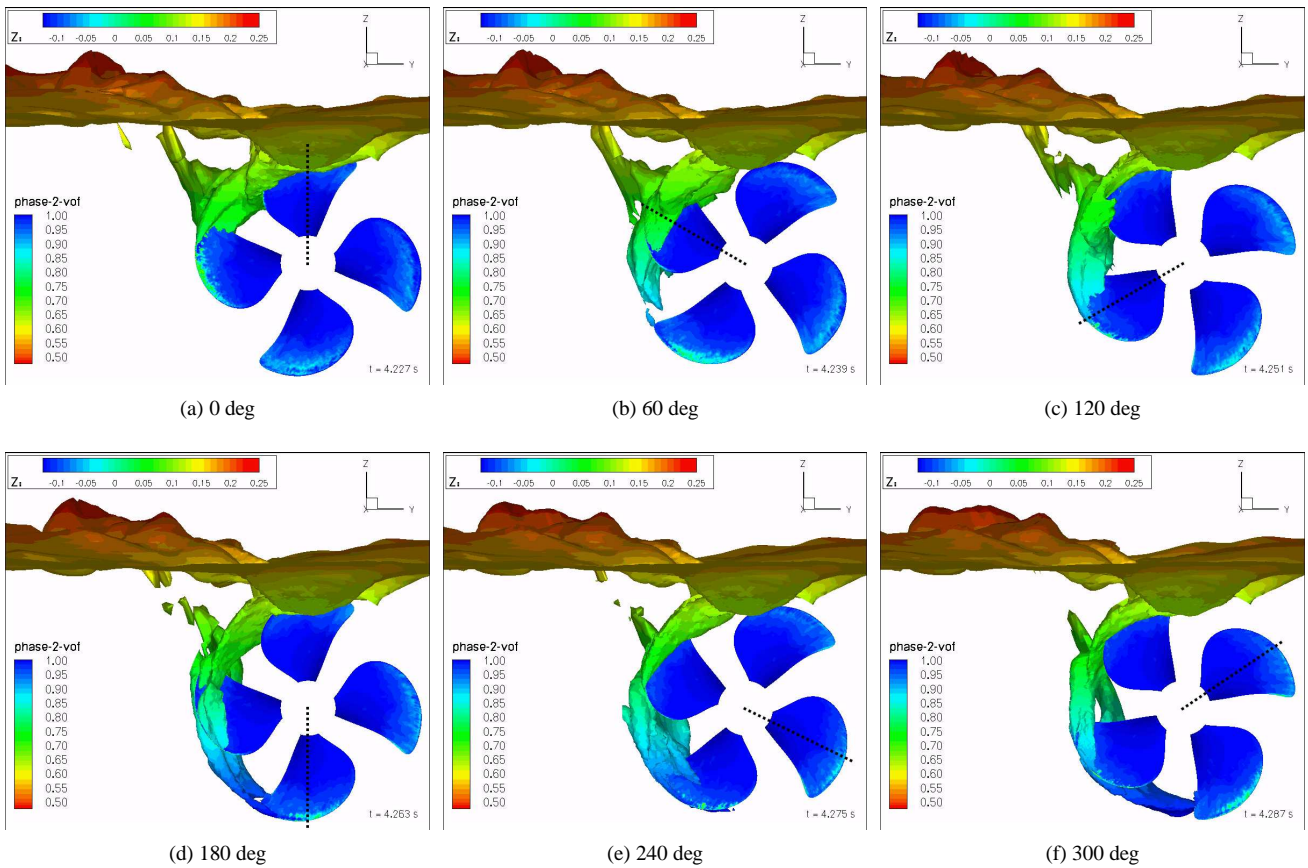


Figure 12: Instantaneous flow fields during one propeller revolution. Propeller blades are colored with water volume fraction, while the free surface with its height position.